International Journal of Advanced Engineering and Technology Research
ISSN: 3106-8677 (Print), ISSN: 3106-8685 (Online) | Vol. 1, No. 2, 2026

Geometric Reinforcement Over Material Upgrading: Integrated Modal–Static–Fatigue Assessment of Large-Scale Hydrogen Cylinder Mounting Systems for Heavy-Duty Commercial Vehicles

Shaaidul Islam [1], Zhangdong Sun [1, 2, *], Xianfeng Li [1], Yian Zhao [1]

[1] School of Automotive Intelligent Manufacturing, Hubei University of Automotive Technology, Shiyan, Hubei 442002, China

[2] Zhengzhou Research Institute of Mechanical Engineering Co., Ltd., Henan 450052, China

[*] **Corresponding author**: (Email: huatzdsun@163.com)

Abstract: When a hydrogen cylinder mounting frame shows signs of inadequate strength, the conventional engineering response is to specify stronger steel. This paper argues that is the wrong diagnosis. Two Q345 frames for a dual-cylinder 510 L hydrogen storage system (1,149 kg total loaded mass) were analysed in Altair OptiStruct and nCode DesignLife under the full ECE R110 inertial load envelope and the ISO 16750-3 road vibration spectrum. The only difference between the two frames was bracket geometry. The baseline frame failed on both counts that matter. Under 6.6g forward loading, stress at the bracket–frame junction reached 396.4 MPa—a yield exceedance of 14.9% for Q345 steel (SF = 0.87). Under road vibration, the longitudinal fatigue damage index reached D = 4.424, more than four times the Palmgren–Miner limit. The two failures share a cause: flat vertical support plates force load transfer through bending rather than axial tension, concentrating stress at a poorly transitioned junction ($K_t \approx 2.8$) whose first natural frequency sits uncomfortably close to the dominant road excitation range. Adding diagonal bracing along the forward load axis and widening fillet radii from R = 5 mm to R = 12 mm resolved both issues without touching the steel specification. Forward stress fell to 214.8 MPa (SF = 1.61); fatigue damage fell to D = 0.004, a reduction of roughly three orders of magnitude. The scale of that improvement may initially look implausible, but it follows directly from IIW FAT 90 weld mechanics: mean stress, RMS amplitude, and stress concentration all fell together, and under the cubic S–N damage law those effects compound multiplicatively rather than adding. For this class of structure, bracket geometry appears to govern fatigue durability more decisively than the steel grade ever could.

Keywords: Hydrogen storage mounting systems, Heavy-duty vehicles, Modal–static–fatigue analysis, Random vibration fatigue, Load-path optimisation, Finite element method, Structural durability.

1. Introduction

1.1. Background and Motivation

There is a structural problem specific to heavy-duty hydrogen fuel cell trucks that lighter platforms simply do not encounter. The cylinders are not small and removable—they are large, permanently welded into the chassis load path for the entire service life of the vehicle. A dual-510 L configuration, once you account for mounting hardware, band straps, piping, and the mass of compressed gas itself, can exceed 1,100 kg. Under ECE R110's 6.6g longitudinal load case—the regulatory stand-in for a hard braking event or frontal collision—that mass generates roughly 74 kN at the four chassis attachment points. That force must be carried elastically, every time the driver brakes. Road vibration layers on a second, slower-acting problem: engine harmonics, surface roughness, and drivetrain excitation combine into broadband vibration across 5–20 Hz throughout service, accumulating fatigue damage over what may be a 10–15 year operational life [7]. Hydrogen FCEVs have taken hold in long-haul trucking and transit bus markets precisely because they offer the refuelling speed and range that battery-electric systems cannot yet match [1-3]. As those deployments scale toward larger vehicles, 510 L Type III vessels at 350 bar have become the standard storage choice, and the structural loading on their mounting frames scales with them. The engineering literature on those frames, however, has not kept pace with the hardware—a gap this study attempts to address.

Type III composite cylinders—aluminium liner, full carbon-fibre overwrap, rated to either 350 or 700 bar depending on the application—have become the standard medium for commercial FCEV storage [4, 5]. Passenger cars typically carry 150–200 L; heavy trucks and buses increasingly run dual 510 L units to reach total capacities above 1,000 L. The structural implications of that size jump are not trivial. The cylinder mass, the inertial forces it generates under ECE R110 loading, and the bending moments those forces impose on the mounting frame all scale in ways that designs derived from passenger-car experience may not anticipate.

ECE R110 [6] was written for compressed natural gas—not hydrogen—but in the absence of a hydrogen-specific mounting standard, the industry has effectively adopted it as the de facto qualification criterion. Its quasi-static acceleration levels (6.6g longitudinal, 5g lateral, 5g vertical) proxy for crash and emergency-braking scenarios. Applied to a system mass of 1,100 kg, those accelerations generate inertial forces approaching 75 kN. What those forces do to the internal stress distribution within the mounting structure—and how that distribution behaves under the additional load of road vibration—is what this analysis addresses.

Regulatory evaluation of such systems commonly follows the inertial loading criteria defined in ECE R110 [6], originally developed for compressed natural gas (CNG) fuel

systems. This regulation specifies quasi-static accelerations of 6.6g longitudinally, 5g laterally, and 5g vertically to simulate crash-equivalent loading conditions. In the absence of hydrogen-specific mounting regulations, these requirements are widely adopted in the hydrogen vehicle industry for structural verification. For a system mass exceeding 1,100 kg, these acceleration levels can generate peak inertial forces approaching 75 kN, producing significant bending moments and stress concentrations within the mounting structure.

Without a clear analytical path through the combined static-fatigue problem, the engineering reflex is to specify stronger steel. Q460 or Q690 instead of Q345 [8]. This is not an unreasonable starting point—it moves the yield threshold without requiring any redesign—but it does not reduce the stress. If a Kt of 2.8 at the bracket junction is what governs failure, then the local stress under a given load is set by the geometry, not by the material choice. Upgrading the steel leaves Kt intact. It also leaves the load path intact, and the natural frequency intact—all three of which appear to be the actual sources of failure in the baseline design examined here. Whether geometry correction alone, with Q345 retained throughout, can bring both static and fatigue performance into compliance is the central question this paper attempts to answer.

1.2. Literature Review and Research Gaps

Published research on hydrogen storage for vehicles has concentrated heavily on the pressure vessel itself — materials, burst mechanics, composite layup optimisation. Its limitation, from the perspective of this study, is where it stops: at the cylinder wall. The steel structure that holds the vessel to the vehicle chassis is treated as outside the scope of the vessel design problem—which is understandable from a pressure-equipment standpoint, but leaves the mounting frame without a comparable analytical treatment.

FE modelling of the vessels themselves is also well developed as a field. Kim et al. [15] validated shell-element burst pressure predictions against physical test data with reasonable agreement; Rafiee and Torabi [16] took this further by propagating manufacturing scatter through the FE model to derive probabilistic burst margins. Vibration fatigue methodology for automotive structures has its own established foundation: Li et al. [17] applied frequency-domain techniques to non-stationary fatigue loading, Benasciutti and Tovo [18] benchmarked spectral methods for random fatigue life prediction across a range of bandwidth conditions, and Bishop and Sherratt [19] provide the foundational treatment for FE-based fatigue calculation that underpins the approach used here. Dirlik's cycle-counting method [31], applied in Section 2.5.3, has been validated against rainflow counting across a range of PSD bandwidths. What is absent from this body of work—conspicuously so, given the safety implications—is any systematic application to hydrogen cylinder mounting frames specifically.

The fatigue method selection is detailed in Section 2.6.4; briefly, Dirlik's empirical cycle-counting method [31] was adopted for its well-documented reliability across PSD bandwidth conditions in automotive contexts, and the IIW FAT 90 S–N class [25] was chosen on the basis of the weld geometry.

Despite this depth of coverage on vessel design and generic vibration fatigue, the literature leaves the hydrogen cylinder mounting frame itself largely unaddressed.

Four specific gaps emerge from this picture. Most published mounting studies address passenger vehicle cylinder sizes — 150–200 L — and the structural implications of scaling to 510 L, with its substantially higher mass and inertial forces, have not been examined [20, 21]. Modal analysis, static strength verification, and vibration fatigue are typically treated as separate analyses rather than a coupled framework, which prevents the resonance proximity identified later in Section 3.1 from being connected causally to the fatigue outcome in Section 3.3. Comparative design studies that quantify the structural performance difference between alternative mounting architectures are essentially absent. And PSD-based fatigue methods, though standard in structural dynamics [22–24], have not been applied to this class of mounting structure.

The four gaps above share a structural root: modal dynamics, static strength, and vibration fatigue tend to be treated as separate analytical exercises, applied to small cylinder configurations, with no cross-design comparison. No single published study appears to have addressed all four within a consistent FE model—a point worth stating plainly, since it is a necessary condition for the kind of causal reasoning this paper attempts. The present analysis does so by using identical boundary conditions, material definitions, and loading inputs for both configurations. The central quantitative finding—a 39% reduction in RMS stress producing a 99.9% reduction in fatigue damage—may not, to the authors' knowledge, have been previously reported for this class of structure. Whether that result generalises beyond this specific configuration is a question worth pursuing.

1.3. Research Objectives and Contributions

This study evaluates two mounting frame designs for a 1,020 L (2 × 510 L) Type III hydrogen cylinder system. The central question is whether geometric reinforcement can replace material upgrading as the design strategy. Both configurations use identical Q345 steel, boundary conditions, and loading inputs. They differ only in bracket geometry, fillet radius, and bracing arrangement. By holding material constant and varying geometry alone, the analysis isolates the contribution of structural architecture to static strength and fatigue durability.

The investigated designs are:

(1) Design-1: A minimalist tubular frame employing a conventional rectangular structural configuration with vertical support plates.

(2) Design-2: An enhanced configuration incorporating reinforced mounting brackets and additional diagonal bracing elements to improve load transfer efficiency and stress redistribution.

The paper makes four specific contributions, each directed at the design strategy question:

(1) An integrated modal–static–fatigue FE framework is developed and applied to a 510 L dual-cylinder mounting system. Running all three analyses on a shared model with identical boundary conditions allows the connections between resonance proximity, static stress, and fatigue damage to be traced directly—something that isolated analyses cannot provide.

(2) A quantitative head-to-head comparison of two structural architectures: a minimalist tubular frame (conventional geometric practice) against a reinforced variant (diagonal bracing, enlarged fillets, modified brackets). The comparison covers static strength, natural frequencies, and

fatigue life under identical loading—allowing the relative contribution of geometry versus material to be clearly separated.

(3) Identification of the physical mechanism behind the 99.9% fatigue improvement: the simultaneous reduction in mean stress, RMS amplitude, and stress concentration factor, whose compound effect under the cubic S–N slope far exceeds what any single change would produce.

(4) Five practical design guidelines extracted from the results, covering load-path alignment, fillet geometry, mean stress control, modal separation, and multi-directional compliance checking. These are stated in terms that a practicing structural engineer can apply directly.

Taken together, the four contributions address a deceptively simple question: can geometry change alone—with no upgrade to the steel—bring a structurally non-compliant mounting frame into full static and fatigue compliance? Based on the analysis presented here, it can. The improvement margin is unexpectedly large: D falls from 4.424 to 0.004, a factor exceeding 1,000, which is considerably larger than a proportional argument would suggest. The reason is the cubic damage exponent of the FAT 90 weld class, which makes the result sensitive to small simultaneous changes in multiple stress parameters. Reporting this mechanism specifically for hydrogen cylinder mounting frames is, as far as the authors can establish, new.

What makes the framework genuinely useful is the sequencing. A single FE model runs modal extraction, ECE R110 static load cases, and ISO 16750-3 PSD fatigue in sequence, using the same mesh, boundary conditions, and material definitions throughout ,so that the modal result feeds directly into the fatigue calculation rather than being treated as a separate exercise.

2. Materials and Methods

2.1. System Configuration

The investigated hydrogen storage assembly consists of two horizontally mounted 510 L Type III composite pressure vessels integrated within a structural steel support frame. The principal system specifications are summarized as follows:

(1) Cylinder capacity: 510 L per cylinder (1,020 L total)

(2) Cylinder technology: Type III (6061-T6 aluminium liner with T700 carbon fiber/epoxy overwrap)

(3) Nominal operating pressure: 350 bar (5,075 psi)

(4) Overall dimensions (per cylinder): Ø650 mm × 1,550 mm (including hemispherical domes; cylindrical section ≈1,100 mm)

(5) Individual cylinder mass: ≈230 kg (empty), ≈250 kg (pressurized)

(6) Total system mass (cylinders + frame + straps + piping + hydrogen): 1,149 kg

The cylinders are supported by steel band straps and mounted to the vehicle chassis through four primary corner connection points. The structural frame is designed to resist both regulatory inertial loading and service-induced vibration.

2.2. Design Configurations

Two structurally distinct mounting concepts were developed and comparatively evaluated.

Design-1: Minimalist Tubular Frame

(1) Rectangular tubular main frame fabricated from Q345 structural steel

(2) Flat vertical support plates

(3) Standard geometric transitions with fillet radius R = 5 mm

(4) Steel band straps fabricated from Q235 steel

(5) Four-point bolted chassis connections

This configuration represents conventional lightweight practice: a bending-dominated load path with R = 5 mm fillet transitions at all major junctions and no supplementary bracing to redirect inertial forces axially.

Design-2: Reinforced Frame with Enhanced Bracing

(1) Reinforced mounting brackets with increased section modulus

(2) Additional diagonal bracing members to improve load redistribution

(3) Enlarged geometric transitions with fillet radius R = 12 mm

(4) Optimized load paths aligned with dominant inertial force directions

(5) Same four-point chassis interface as Design-1

This configuration converts the bending-dominated load transfer of Design-1 into a predominantly axial mechanism: diagonal bracing aligned with the forward inertial vector, combined with enlarged bracket fillets (R = 12 mm), establishes multiple parallel axial load paths and reduces stress concentration at the critical junction.

2.3. Material Properties and Fatigue Parameters

Structural materials were selected in accordance with GB/T 1591-2018 and GB/T 700-2006 standards. The mechanical properties adopted in the finite element model are summarized in Table 1.

Table 1. Material Properties

Property	Q345 Steel (Frame)	Q235 Steel (Straps)	Units
Elastic modulus, E	210	210	GPa
Yield strength, σ_y	345	235	MPa
Ultimate tensile strength, σ_u	470-630	370-500	MPa
Poisson's ratio, ν	0.30	0.30	-
Density, ρ	7,850	7,850	kg/m³

Fatigue properties were derived from the IIW Recommendations for Fatigue Design of Welded Joints and Components [25]. The stress–life relationship follows the Basquin power-law form:

$$N = \frac{C}{(\Delta\sigma)^m} \quad (1)$$

Where:

(1) N= cycles to failure

(2) $\Delta\sigma$= stress range (MPa)

(3) $m = 3$= fatigue strength exponent for welded steel details

(4) $C = 1.46 \times 10^{12}$(MPa³·cycles), back-calculated from FAT 90 at 2×10^6cycles

The characteristic fatigue strength $\Delta\sigma_c = 90$MPa at 2×10^6cycles corresponds to IIW FAT 90 for as-welded fillet attachments and longitudinal welds [25].

Because IIW nominal stress curves are defined at a stress ratio of approximately $R \approx 0.5$, implicitly accounting for high tensile residual stresses typical of welded joints, no additional Goodman correction was applied in the fatigue

damage integration, consistent with IIW recommendations [25].

2.4. Finite Element Modeling

All analyses were performed using Altair OptiStruct with fatigue post-processing conducted in nCode DesignLife [33].

2.4.1. Mesh Generation and Convergence Verification

Four-node quadrilateral shell elements (CQUAD4) with triangular elements (CTRIA3) at geometric transitions were employed, consistent with the thin-walled tubular construction of the mounting frame. Mesh convergence was verified through progressive refinement, reducing the global element size from 15 mm to 5 mm in stress-critical regions.

Convergence was considered achieved when the maximum von Mises stress variation between successive refinements was less than 3%.

Final mesh statistics:

(1) Design-1: ≈285,000 elements; ≈98,000 nodes

(2) Design-2: ≈312,000 elements; ≈106,000 nodes

Element quality metrics confirmed that more than 98% of elements satisfied standard shell quality criteria (aspect ratio < 5; warpage < 5°; skew angle < 60°; Jacobian > 0.7).

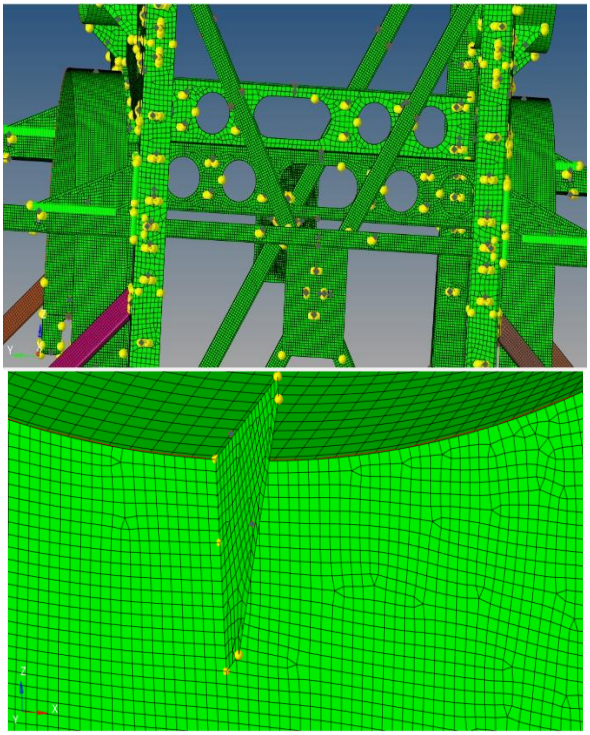

Figure 1. FE mesh of the hydrogen cylinder mounting frame. (a) Assembly view: quad-dominant CQUAD4 shell elements with local refinement at member junctions, hole perimeters, and bracket interfaces; yellow spheres mark RBE2 rigid elements at the four bolted chassis attachment points. (b) Close-up at the cylinder–bracket fillet: the mesh grades from the global 15 mm region down to 5 mm at the curved transition, which is the primary stress concentration site in both designs.

2.4.2. Boundary Conditions and Contact Modeling

Chassis mounting constraints:

All six degrees of freedom were constrained at the four corner mounting interfaces, representing rigid bolted connections to the vehicle chassis.

Cylinder–strap interaction:

Surface-to-surface contact was defined with a friction coefficient μ = 0.45 for dry steel–aluminium contact [26], implemented using the augmented Lagrangian formulation.

Strap fastening representation:

Strap ends were modeled using rigid body elements (RBE2), approximating bolted joint load transfer behavior.

2.5. Analysis Procedures

2.5.1. Modal Analysis

Free vibration characteristics were extracted by solving the eigenvalue problem:

$$[K]\{\phi\} = \omega^2[M]\{\phi\} \quad (2)$$

Using the Lanczos eigen-solution algorithm [27]. Natural frequencies and corresponding mode shapes were obtained to identify potential resonance risk within the operating frequency range.

2.5.2. Static Strength Analysis

Quasi-static inertial loading was applied in accordance with ECE R110 [6].

Applied forces:

$$F_x = 1{,}149 \times (6.6 \times 9.81) = 74{,}393 \text{ N} \quad (3)$$

$$F_y = F_z = 1{,}149 \times (5.0 \times 9.81) = 56{,}357 \text{ N} \quad (4)$$

Structural acceptance criterion:

$$\sigma_{VM} < \sigma_y = 345 \text{ MPa} \quad (5)$$

The safety factor is defined as:

$$SF = \frac{\sigma_y}{\sigma_{VM}} \quad (6)$$

Compliance is satisfied when $SF > 1.0$, consistent with ECE R110 regulatory requirements [6].

2.5.3. Random Vibration Fatigue Analysis

Frequency-domain stress–life methodology was employed for random vibration fatigue assessment [28, 29].

Representative acceleration PSD inputs were defined according to ISO 16750-3 [30] and are summarized in Table 2, resulting in a total tri-axial RMS acceleration of 1.36 g.

Table 2. Input PSD Spectrum (Representative Values)

Frequency (Hz)	X-axis PSD (g^2/Hz)	Y-axis PSD (g^2/Hz)	Z-axis PSD (g^2/Hz)
5	0.050	0.051	0.020
10	0.060	0.051	0.025
20	0.060	0.051	0.030
50	0.010	0.008	0.008
100	0.003	0.002	0.002
200	0.0004	0.0008	0.0005

The stress PSD at any structural location was obtained via:

$$G_\sigma(f) = |H(f)|^2 \cdot G_{acc}(f) \quad (7)$$

Where $H(f)$ is the frequency response function and $G_{acc}(f)$is the input acceleration PSD.

A structural damping ratio of ζ = 2% was assumed, consistent with bolted welded steel assemblies [22].

The signed von Mises stress—preserving the sign of the principal stress with largest absolute magnitude—was used as the fatigue stress metric, appropriate for uniaxially dominated vibration problems [19].

Cycle counting was performed using Dirlik's empirical method [31]. The static stress field from the 6.6g forward load case was imported into nCode DesignLife as a nodal mean stress offset. The dynamic stress amplitude distribution derived from the PSD was combined with this mean stress

during S–N damage integration.

Because the IIW FAT 90 curve is defined at $R \approx 0.5$, implicitly representing worst-case residual stress conditions, no additional Goodman correction was applied [25].

Fatigue damage accumulation followed the Palmgren–Miner linear damage rule [32]:

$$D = \sum \frac{n_i}{N_{f,i}} \quad (8)$$

Failure is predicted when $D \geq 1.0$.

All fatigue calculations were conducted in nCode DesignLife [33] coupled with Altair OptiStruct.

2.6. Model Verification and Validation Strategy

FE models of this type carry assumptions that can produce plausible-looking but unreliable results if left unchecked. Four independent verification checks were carried out before the results were used for any comparative interpretation.

2.6.1. Mesh Convergence Verification

Mesh convergence was checked by refining from 15 mm global to 5 mm local elements at stress-critical locations. Convergence was declared when successive refinements changed the peak von Mises stress by less than 3%.

2.6.2. Static Load Verification

Applied inertial forces were verified by hand calculation: F = m×a applied to the 1,149 kg total system mass at each ECE R110 acceleration level. Summing reaction forces at the constrained nodes confirmed equilibrium to within 1%.

2.6.3. Modal Solution Consistency

The extracted natural frequencies were verified for numerical stability by:

(1) Comparing the first three modes under refined mesh levels

(2) Confirming modal orthogonality

(3) Ensuring effective mass participation exceeded 90% in principal directions

When all three checks are satisfied, the extracted natural frequencies can be attributed to the structural geometry rather than discretisation artefacts.

2.6.4. Fatigue Method Validation

Dirlik's method [31] was selected partly for practical reasons—it is well-implemented in nCode DesignLife—but also because it has been systematically compared against time-domain rainflow counting across a wide range of Gaussian bandwidth conditions and tends to perform well precisely in the broadband PSD environments typical of road vehicle applications. The IIW FAT 90 S–N classification was selected on the basis of the weld geometry: fillet attachments to a main member loaded in bending perpendicular to the weld toe. Mean stress was not corrected separately because the FAT 90 curve is already derived at R ≈ 0.5, which implicitly captures the high tensile residual stresses that characterise as-welded joints [25]. The 2% damping assumption is consistent with published measurements for bolted welded steel frames [22]; its sensitivity is discussed in Section 4.7.

The IIW FAT 90 S–N curve selection and damage integration procedure follow IIW Recommendations for welded steel structures [25]. The use of the Palmgren–Miner linear damage rule [32] is consistent with standard engineering practice for high-cycle fatigue assessment.

Structural damping was set to 2%, which is within the measured range for bolted welded steel [22].

2.6.5. Modeling Assumptions and Limitations

Several simplifying assumptions were made:

(1) Linear elastic material behavior

(2) Small deformation theory

(3) Uniform structural damping

(4) Gaussian stationary random vibration input

Hydrogen embrittlement, weld residual stresses, and contact slip at the cylinder–strap interface were all left outside the model scope. These are not small effects in an absolute sense—residual stresses in particular can be significant fractions of yield—but for a comparative study where both configurations share the same material, joint type, and fabrication assumptions, their exclusion may be more defensible. Whether that defence holds depends on how different the two designs are in terms of weld quality and joint geometry, which is a question worth examining in subsequent experimental work.

3. Results

3.1. Modal Characteristics — Design-1

Table 3 lists the first six natural frequencies and associated modal characteristics for Design-1. Six modes are enough to capture over 85% of effective mass in each principal direction, which is considered adequate for the frequency range of interest. What matters most from a fatigue perspective is not the modal completeness metric—it is where Modes 1 and 2 sit relative to the road vibration spectrum.

Table 3. Natural Frequencies and Modal Characteristics - Design-1

Mode	Frequency (Hz)	Effective Mass (%)	Mode Description
1	25.0	47.3 (Y-direction)	Primary lateral bending, global frame deformation
2	26.0	42.1 (X-direction)	Longitudinal bending, cylinder-frame motion
3	38.2	8.7 (Z-direction)	Torsional mode about longitudinal axis
4	38.9	12.4 (Y-direction)	Secondary lateral mode with local plate bending
5	39.3	6.2 (X-direction)	Vertical support plate vibration
6	41.5	9.8 (combined)	Coupled frame-cylinder mode

Mode 1 at 25.0 Hz moves the whole frame-cylinder assembly laterally (47.3% effective mass in Y). Mode 2 at 26.0 Hz is longitudinal bending with cylinder-frame coupling (42.1% in X). The two modes are only 1 Hz apart, which under broadband excitation means they can interact.

Cumulative effective mass reaches 89.7% in X, 91.4% in Y, and 87.3% in Z across the first six modes. That is sufficient modal representation for the frequency range of interest.

The difficulty with 25–26 Hz is precisely its proximity to the road excitation band. ISO 16750-3 concentrates most PSD energy below 20 Hz, placing Modes 1 and 2 only 5–6 Hz above the high-energy region. That separation may seem

adequate on paper, but welded steel assemblies typically show natural frequency scatter of ±5–10% due to manufacturing variation [22]. In the worst production case, the margin could close to 2–3 Hz—and at 2% structural damping, 2 Hz separation is close enough to produce meaningful resonance amplification. This is consistent with what the fatigue analysis reveals: a forward RMS stress of 106.6 MPa, which is considerably higher than the quasi-static results alone would suggest.

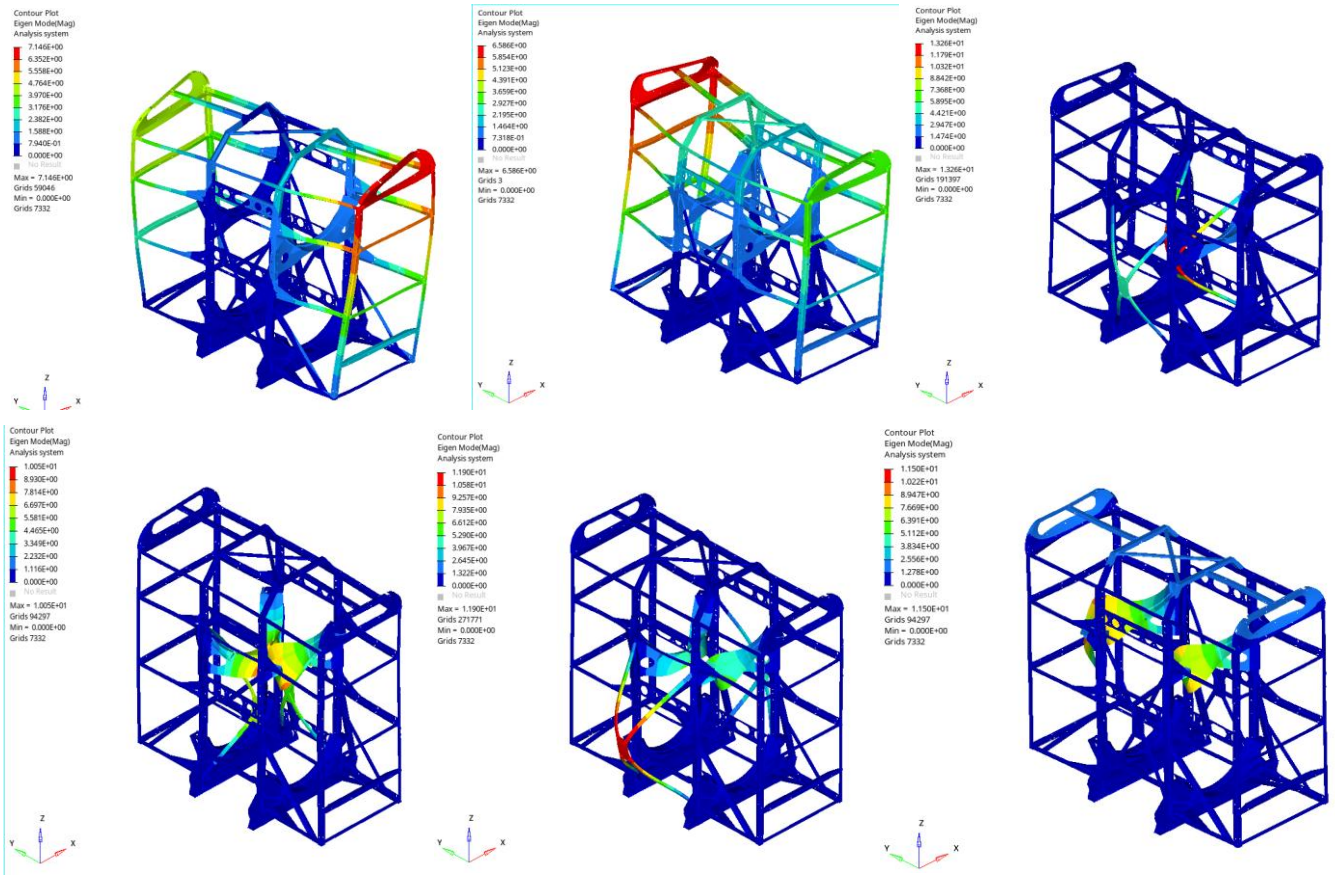

Figure 2. First six mode shapes for Design-1 (displacement magnitude colour scale). Mode 1 at 25.0 Hz: global lateral bending, 47.3% effective mass (Y). Mode 2 at 26.0 Hz: longitudinal bending with cylinder–frame coupling, 42.1% (X). Modes 3–6 fall between 38.2 and 41.5 Hz: torsion, secondary lateral bending, vertical plate vibration, and a coupled frame–cylinder mode. Cumulative effective mass participation exceeds 87% in all three principal directions across these six modes.

The extracted natural frequencies overlaid on the operational PSD spectrum:

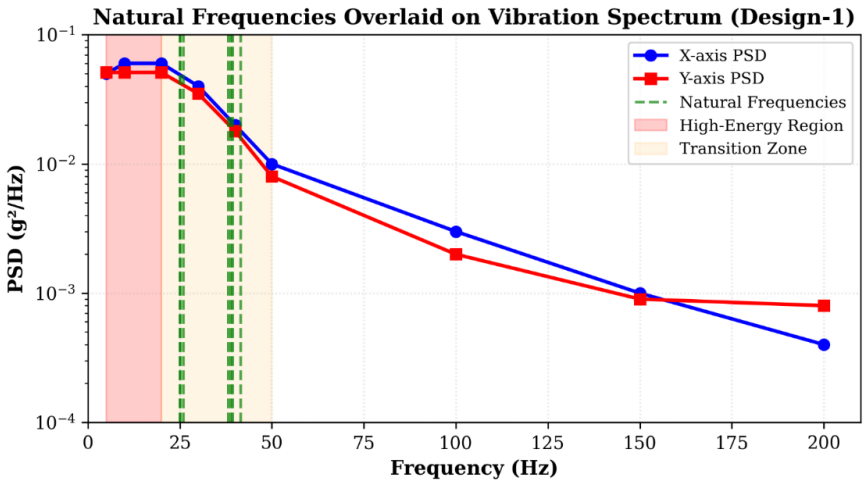

Figure 3. Design-1 natural frequencies (vertical dashed lines) plotted against the ISO 16750-3 PSD input spectrum. Modes 1 and 2 at 25–26 Hz lie only 5–6 Hz above the high-energy excitation region (5–20 Hz, shaded). Modes 3–6 at 38–42 Hz fall in the PSD decay region. The proximity of the first two modes to the energetic band is the primary driver of resonance amplification and the elevated RMS stress observed in Section 3.3.1.

3.2. Static Strength Performance

3.2.1. Design-1: Minimalist Tubular Frame

Static strength results under quasi-static inertial loading per ECE R110 [6] are summarised in Table 4. From an engineering perspective, the forward loading case is the critical one—the 6.6g acceleration applied to 1,149 kg

produces the largest bending moment at the mounting bracket.

Table 4. Static Strength Results - Minimalist Tubular Frame Design

Load Case	Max Displacement (mm)	Max von Mises Stress (MPa)	Critical Location	Safety Factor	Status
Forward 6.6g	7.024	396.433	Bottom mounting plate-frame interface	0.87	FAIL
Lateral 5g	2.364	281.500	Vertical support plate edge	1.23	marginal but acceptable performance
Vertical 5g	0.637	57.468	Frame support junction	6.00	PASS

Under forward 6.6g loading, the critical location reaches 396.4 MPa. Q345 structural steel yields at 345 MPa, placing that result 14.9% above the elastic limit. The safety factor of 0.87 indicates that the design is already operating in the plastic range before any road vibration is overlaid—not a comfortable starting point for a fatigue-sensitive structure.

Three factors converge to produce that stress level. First, the cylinder centre of gravity sits above the lower frame rail, so a forward inertia load arrives at the mounting plate as a bending moment rather than a clean axial pull. Second, that bending moment must transfer across the vertical support plate junction, a cross-section change that introduces additional bending and stress concentration. Third, the 5 mm fillet at that junction yields $K_t \approx 2.8$ by Peterson's charts [35]—amplifying an already unfavourably loaded section. The combination of bending-dominated load path, cross-section transition, and high Kt is what drives the local stress 14.9% above yield.

(1) Load path eccentricity between cylinder center of mass and lower frame rail

(2) Local stress concentration at the vertical support plate junction

(3) Insufficient section modulus of the rectangular tubular member

Although lateral loading remains marginally within elastic limits (SF = 1.23), the forward case clearly violates regulatory strength requirements. Vertical loading is non-critical.

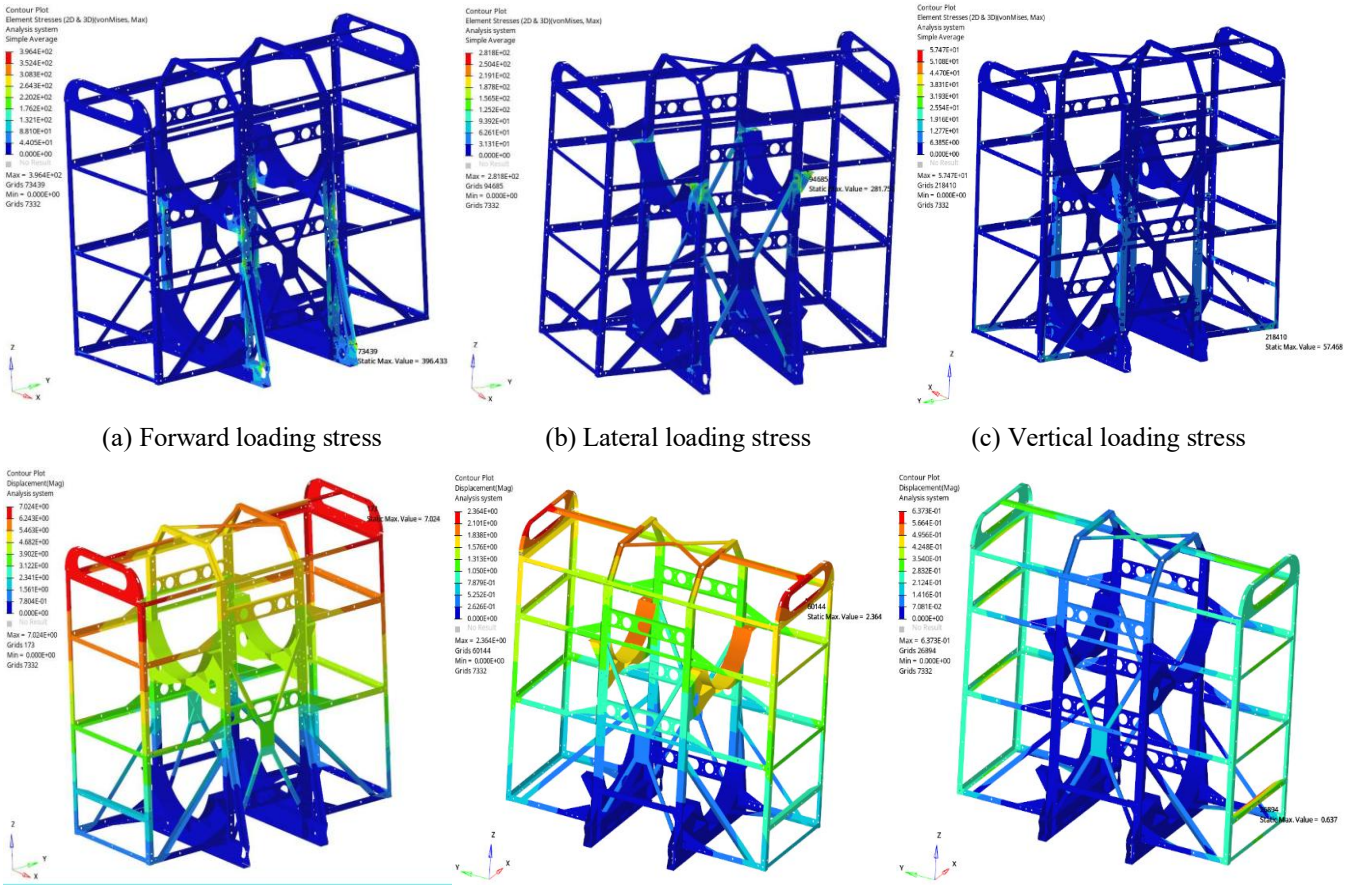

(a) Forward loading stress (b) Lateral loading stress (c) Vertical loading stress

(d) Forward displacement (e) Lateral displacement (f) Vertical displacement

Figure 4. Design-1 static results under ECE R110 quasi-static loading. (a–c) Von Mises stress contours for forward 6.6g, lateral 5g, and vertical 5g cases: peak forward stress 396.4 MPa (FAIL, 14.9% above Q345 yield), lateral 281.5 MPa (SF = 1.23), vertical 57.5 MPa (SF = 6.00). The critical failure site is the bottom mounting plate–frame interface. (d–f) Corresponding displacement contours: 7.0 mm forward, 2.4 mm lateral, 0.6 mm vertical. Stress in MPa, displacement in mm.

3.2.2. Design-2: Reinforced Frame

Static strength results for Design-2 are summarized in Table 5.

Table 5. Static Strength Results - Reinforced Frame Design

Load Case	Max Displacement (mm)	Max von Mises Stress (MPa)	Critical Location	Safety Factor	Status
Forward 6.6g	7.510	214.826	Reinforced mounting bracket	1.61	PASS
Lateral 5g	3.743	335.762	Frame corner connection	1.03	PASS
Vertical 5g	1.026	42.825	Strap attachment region	8.06	PASS

Design-2 passes all three load cases. Forward peak stress drops from 396.4 to 214.8 MPa, a 45.8% reduction, moving the safety factor from 0.87 to 1.61. The other two directions stay within limits.

This improvement results from:

(1) Increased local section modulus at the mounting bracket

(2) Improved force transmission through diagonal bracing

(3) Reduction of stress concentration at the plate–frame junction

Lateral stress goes up slightly: 281.5 to 335.8 MPa (+19.3%). The diagonal bracing is oriented for forward loads, so it introduces some transverse eccentricity. The lateral safety factor drops to 1.03—still above the ECE R110 minimum, but with limited margin.

This lateral stress increase is an inherent trade-off of bracing oriented for the dominant forward load: addressing the critical failure direction introduces modest transverse eccentricity, but the resulting SF of 1.03 remains within ECE R110 limits.

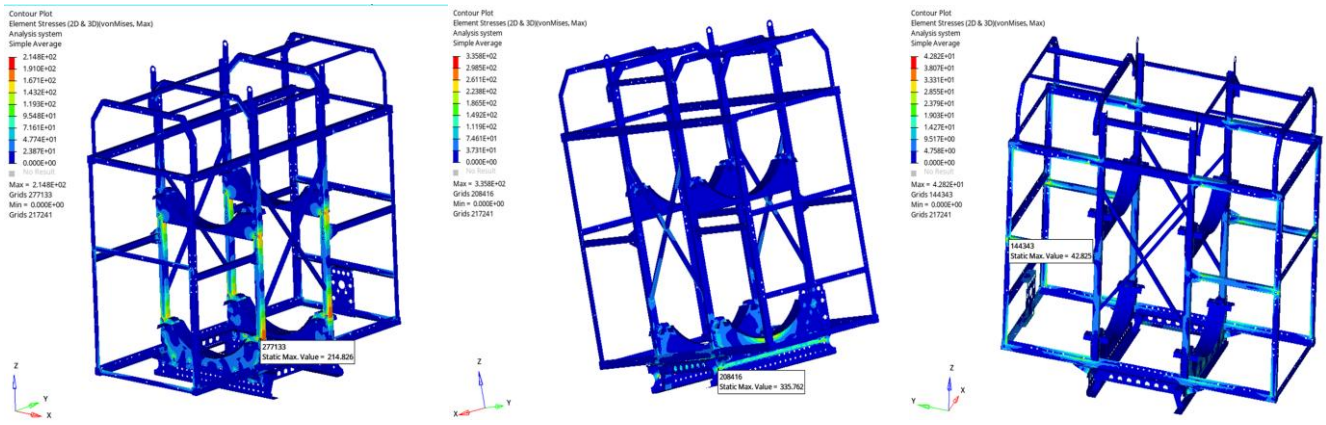

(a)Forward loading stress (b) Lateral loading stress (c) Vertical loading stress

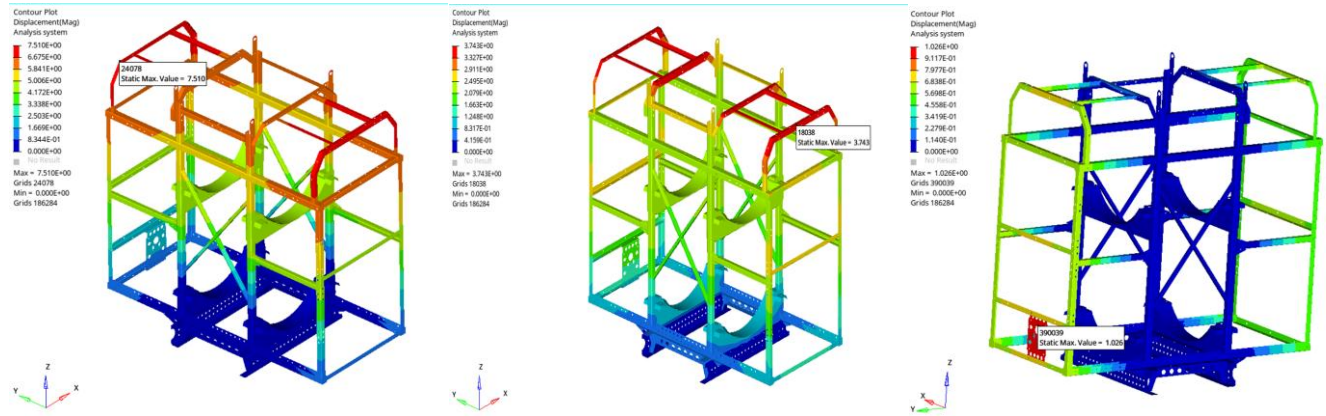

(d) Forward displacement (e) Lateral displacement (f) Vertical displacement

Figure 5. Design-2 static results under ECE R110 loading. (a–c) Von Mises stress contours: forward 214.8 MPa (SF = 1.61, PASS), lateral 335.8 MPa (SF = 1.03), vertical 42.8 MPa (SF = 8.06) — all three directions comply with the Q345 yield criterion. Forward peak stress is 45.8% lower than Design-1 despite slightly higher maximum displacement, reflecting load redistribution across multiple members rather than concentration at a single junction. (d–f) Displacement contours: 7.5 mm forward, 3.7 mm lateral, 1.0 mm vertical. Stress in MPa, displacement in mm.

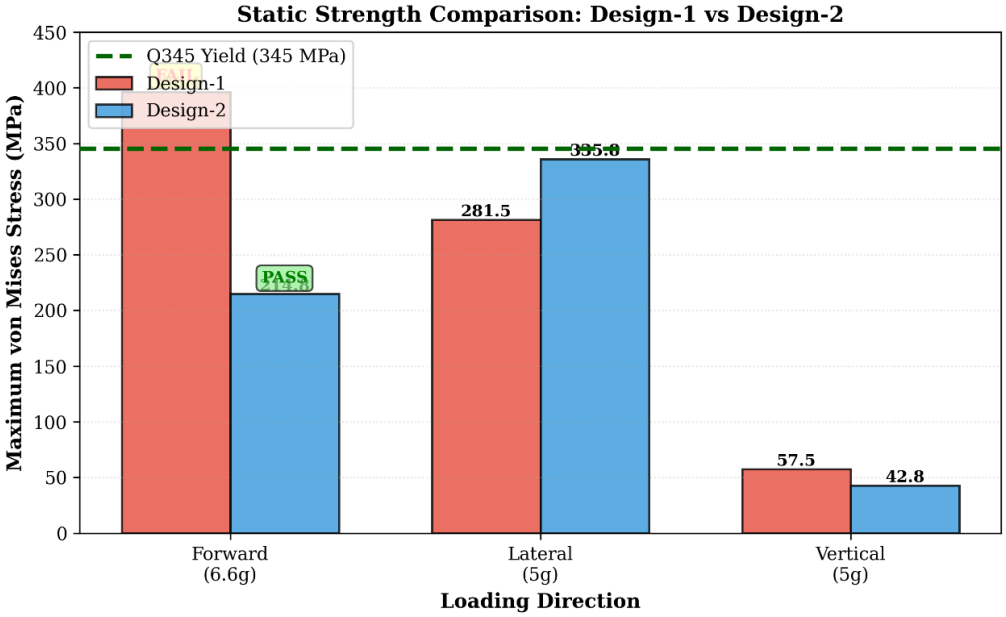

Figure 6. Peak von Mises stress comparison: Design-1 (red) vs Design-2 (blue) across three ECE R110 load directions. The horizontal dashed line marks the Q345 yield limit (345 MPa). Design-1 exceeds this limit in the forward direction (396.4 MPa, FAIL). Design-2 complies in all three directions; forward stress drops by 45.8% to 214.8 MPa. Lateral stress rises modestly in Design-2 (281.5 → 335.8 MPa, +19.3%) due to the bracing orientation, but SF remains above 1.0.

3.3. Random Vibration Fatigue Performance

3.3.1. Design-1: Minimalist Frame

Fatigue results derived using frequency-domain methodology and Dirlik cycle counting [31] are presented in Table 6. It should be noted that the damage values here are dimensionless cumulative damage indices under continuous PSD excitation—D = 1.0 marks the failure threshold under Palmgren–Miner summation.

Table 6. Vibration Fatigue Results - Minimalist Tubular Frame Design

Direction	RMS Stress (MPa)	Fatigue Damage	Time to D=1.0* (s)	Critical Location	Status
Forward (X)	106.634	4.424	49.442	Vertical plate-frame junction	FAIL
Lateral (Y)	83.432	0.160	1,045.873	Side rail connection	PASS
Vertical (Z)	9.325	0.000	8.696×10^{15}	Strap interface (negligible)	PASS

Longitudinal fatigue damage is D = 4.424, against an acceptance limit of D = 1.0—a factor-of-4.4 exceedance that leaves no room for uncertainty. Design-1 fails the fatigue criterion comprehensively.

Three factors converge at the plate–frame junction. The static mean stress of 396.4 MPa consumes the entire elastic range of Q345 before any dynamic loading is added. Near-resonance amplification near 25 Hz then imposes a superimposed RMS stress of 106.6 MPa, confirmed by the FRF-weighted PSD calculation. Geometric stress concentration ($K_t \approx 2.8$) amplifies both components at the same location. Because IIW FAT 90 damage accumulates in proportion to stress amplitude cubed (m = 3), even a moderate dynamic amplitude at high mean stress produces fatigue damage at a rate that intuition tends to underestimate significantly.

(1) High static mean stress (396.4 MPa baseline)
(2) Resonance amplification near 25 Hz
(3) Geometric stress concentration ($K_t \approx 2.8$)

The 106.6 MPa RMS stress is higher than quasi-static analysis alone would suggest—evidence of dynamic amplification near the first natural frequency. Since IIW FAT 90 damage scales with σ^3, a moderate RMS reduction produces a much larger damage reduction.

Lateral and vertical directions remain below the failure threshold.

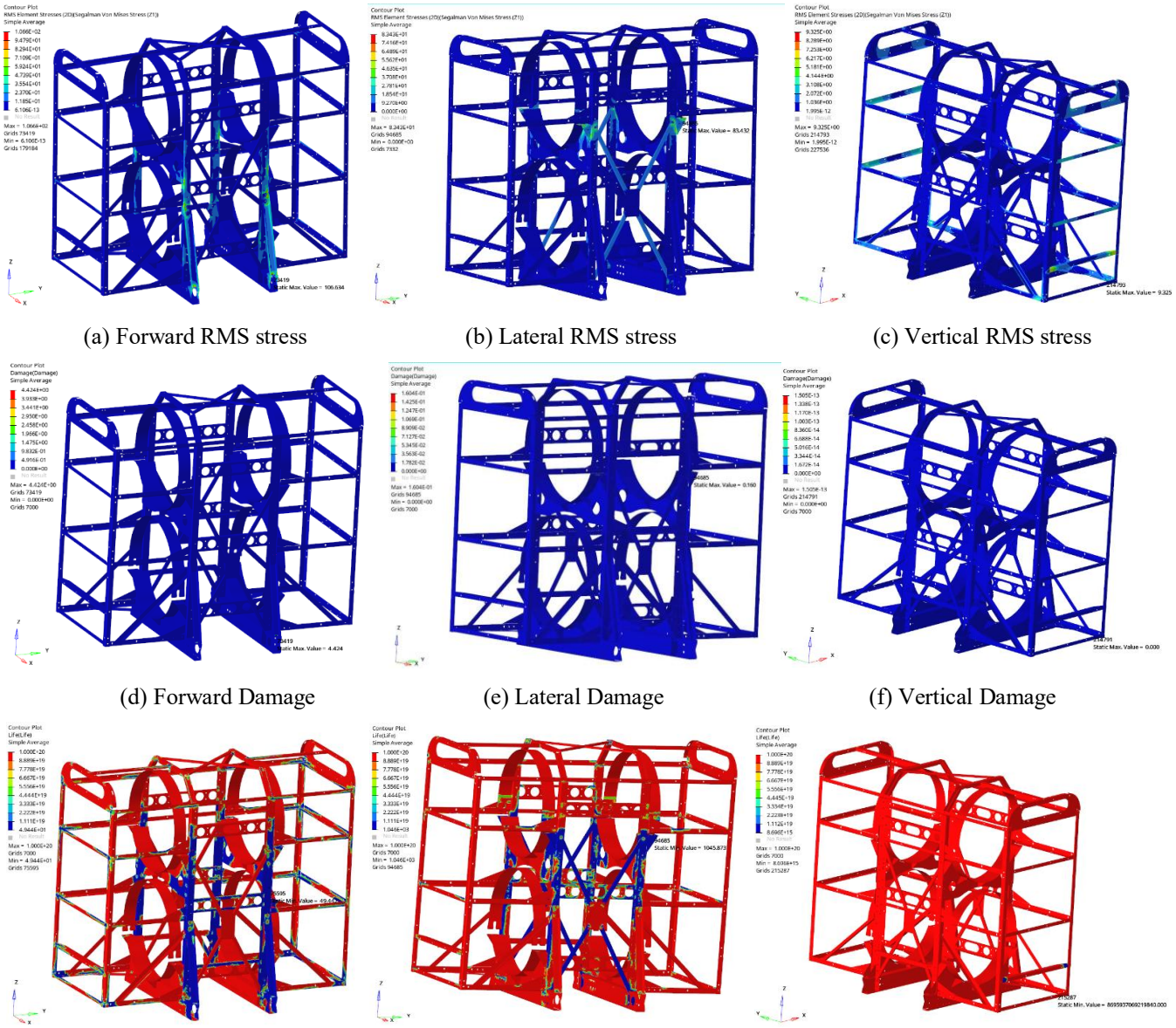

(a) Forward RMS stress (b) Lateral RMS stress (c) Vertical RMS stress

(d) Forward Damage (e) Lateral Damage (f) Vertical Damage

(g) Forward life (h) Lateral life (i) Vertical life

Figure 7. Vibration fatigue results for Design-1 under ISO 16750-3 PSD excitation. (a–c) RMS stress contours: forward 106.6 MPa, lateral 83.4 MPa, vertical 9.3 MPa. The forward RMS is substantially higher than quasi-static analysis would predict, reflecting resonance amplification near 25 Hz. (d–f) Fatigue damage index contours: forward D = 4.424 (FAIL — 4.4 times the D = 1.0 limit), lateral D = 0.160, vertical D ≈0. (g–i) Predicted time to D = 1.0: 49.4 s forward, 1,045.9 s lateral, 8.7×10^{15} s vertical. The forward failure is driven by three compounding factors: static mean stress at 396.4 MPa, near-resonance amplification, and Kt ≈ 2.8.

3.3.2. Design-2: Reinforced Frame

Fatigue results for Design-2 are summarized in Table 7.

Table 7. Vibration Fatigue Results - Reinforced Frame Design

Direction	RMS Stress (MPa)	Fatigue Damage	Time to D=1.0* (s)	Critical Location	Status
Longitudinal	64.687	0.004	452.561	Modified mounting bracket	PASS
Transverse	87.459	0.044	684.137	Frame connection	PASS
Vertical	9.127	0.000	6.766×10^{13}	Strap interface (negligible)	PASS

Design-2 achieves fatigue compliance in all three load directions. Longitudinal RMS stress falls to 64.7 MPa, a 39.3% reduction from the baseline. The corresponding damage index falls to D = 0.004, a 99.9% reduction. A 39% stress improvement producing a 99.9% damage improvement might appear to be an analytical artefact; it is not. It is the straightforward consequence of the m = 3 damage exponent, under which a 39% reduction in amplitude translates to a damage ratio of $0.61^3 \approx 0.23$—and that is before accounting for the simultaneous reductions in mean stress and Kt, whose effects multiply further.

Three quantities all dropped together: mean stress (396.4→214.8 MPa), RMS amplitude (106.6→ 64.7 MPa), and Kt (2.8→1.9). In the Palmgren–Miner damage sum with m = 3, those reductions multiply rather than add. That is why the overall damage ratio goes from 4.424 to 0.004—250 times below the failure threshold.

(1) Reduced dynamic stress amplitude

(2) Substantially lower mean stress

(3) Decreased stress concentration factor (Kt ≈ 1.9)

Due to the cubic slope (m = 3) of the IIW S–N curve [25], fatigue damage reduction scales nonlinearly with stress reduction, explaining the dramatic improvement.

The resulting damage index (0.004) provides approximately 250× margin relative to the failure threshold (D = 1.0), indicating substantial fatigue margin under the prescribed vibration conditions.

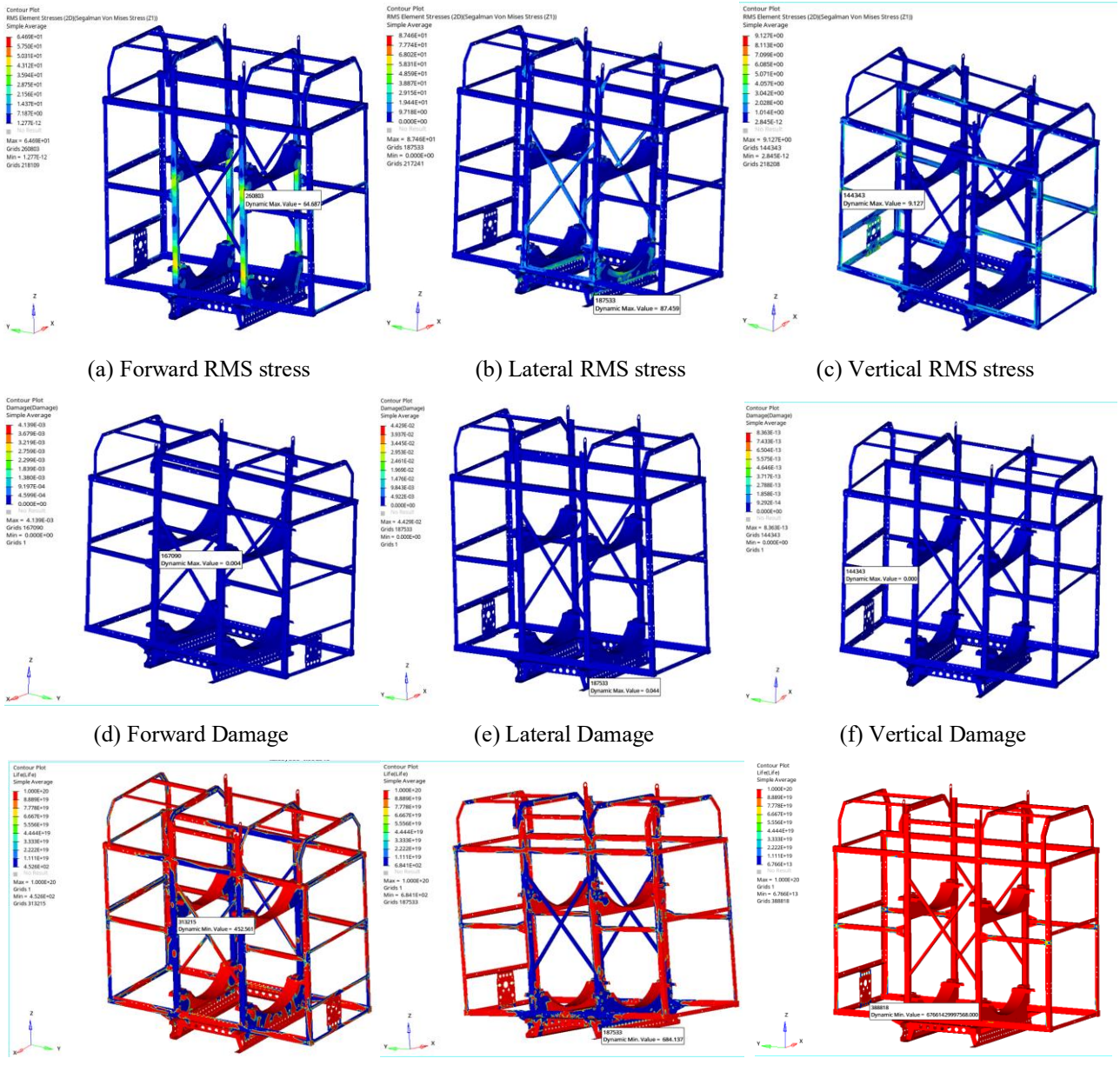

(a) Forward RMS stress (b) Lateral RMS stress (c) Vertical RMS stress

(d) Forward Damage (e) Lateral Damage (f) Vertical Damage

(g) Forward Life (h) Lateral Life (i) Vertical Life

Figure 8. Vibration fatigue results for Design-2 under the same ISO 16750-3 PSD input. (a–c) RMS stress contours: longitudinal 64.7 MPa (39% lower than Design-1), transverse 87.5 MPa, vertical 9.1 MPa. (d–f) Fatigue damage contours: longitudinal D = 0.004 (250× below the D = 1.0 limit, PASS), transverse D = 0.044, vertical D ≈0. All three directions comply. (g–i) Predicted time to D = 1.0: 452.6 s longitudinal, 684.1 s transverse, 6.8×10^{13} s vertical. The 99.9% longitudinal damage reduction from a 39% RMS stress reduction reflects the simultaneous decrease in mean stress, RMS amplitude, and Kt, whose combined effect on the cubic S–N damage integral is multiplicative.

3.4. Integrated Structural Performance Comparison

A consolidated performance comparison between the two configurations is provided in Table 8.

Table 8. Overall Performance Comparison

Performance Metric	Minimalist Frame (Design-1)	Reinforced Frame (Design-2)	Improvement
STATIC STRENGTH			
Forward stress (MPa)	396.4	214.8	-45.8%
Lateral stress (MPa)	281.5	335.8	+19.3%
Vertical stress (MPa)	57.5	42.8	-25.5%
Minimum safety factor	0.87	1.03	+18.4%
Q345 compliance	NO	YES	ACHIEVED
Required material	Q460/Q500	Q345	1 grade lower
VIBRATION FATIGUE			
Forward/Long. RMS (MPa)	106.6	64.7	-39.3%
Forward/Long. damage	4.424	0.004	-99.9%
Lateral/Trans. damage	0.160	0.044	-72.5%
Vertical damage	~0	~0	-
All directions pass	NO	YES	ACHIEVED
Worst-case margin	-342%	+99.6%	+442 points
MODAL BEHAVIOR			
1st natural freq. (Hz)	25.0		-
Resonance risk	Moderate		-

Design-1 fails both static forward loading and longitudinal vibration fatigue criteria. Design-2 satisfies all three:

(1) Yield strength requirements in all directions

(2) Fatigue damage criterion ($D < 1.0$) in all axes

(3) Acceptable displacement levels

Geometry change resolved both failures simultaneously. A material upgrade would have raised the yield threshold but left the load path, stress concentration, and resonance frequency unchanged—the actual causes of failure. Geometry change addresses all three at once.

(1) 45.8% reduction in forward static stress

(2) 39.3% reduction in longitudinal RMS stress

(3) 99% reduction in fatigue damage

Mass was not tracked explicitly in the present models, but the added material consists of diagonal bracing members and thickened bracket plates rather than a wholesale frame upsize. The intent is load-path correction rather than mass addition, consistent with the stress reduction pattern observed across all loading directions.

Running modal, static, and fatigue analyses on a single consistent model reveals connections that isolated analyses obscure. The resonance proximity identified in Section 3.1 is directly traceable to the fatigue amplification in Section 3.3.1—a causal chain that only becomes visible when the modal result feeds the fatigue calculation on the same mesh.

This integration is the methodological contribution: each analysis stage informs the next, and the combined result is qualitatively different from the sum of three independent studies.

3.5. Modal Characteristics — Design-2 (Reinforced Configuration)

Full modal extraction was not performed for Design-2 in this study. The fatigue calculation in Section 3.3.2 implicitly uses the reinforced configuration's frequency response functions, so its dynamic behaviour is accounted for in the damage results. Qualitative interpretation of what the reinforcement does to the mode shapes can be drawn from structural mechanics principles, as described below.

The addition of diagonal bracing members, reinforced mounting brackets, and enlarged fillet radii (R = 12 mm) increases global and local structural stiffness without proportional mass addition. According to the eigenvalue relationship $\omega = \sqrt{(K/M)}$, an increase in effective stiffness K with approximately constant mass M produces an upward shift in natural frequencies.

The reinforced configuration is therefore expected to exhibit a higher first natural frequency than the 25 Hz identified for Design-1, resulting in improved separation from the dominant excitation band (5–20 Hz per ISO 16750-3). This expectation is supported by the observed 39.3% reduction in longitudinal RMS stress under identical PSD excitation (Section 3.3.2), which is consistent with reduced resonance amplification.

Explicit modal reporting for Design-2 is left for follow-up work, where experimental validation of natural frequencies would also be of value.

4. Discussion

4.1. Structural Deficiencies of the Minimalist Configuration

4.1.1. Load Path Inefficiency and Bending-Dominated Response

At 1,149 kg total mass under 6.6g longitudinal deceleration, the mounting frame must transfer roughly 74 kN from the cylinder centroids to four chassis points. In Design-1, that transfer goes almost entirely through bending in the vertical support plates. Bending stress grows with load eccentricity and the inverse of section modulus, both of which are unfavourable here: 4 mm plates loaded about their weak axis, with the cylinder CG above the lower frame rail, introduce a moment arm that forces load transfer through bending. The 5 mm fillet at the plate–frame junction yields $K_t \approx 2.8$ by Peterson's charts [35], concentrating the already-elevated bending stress at exactly where two members meet and load must cross a section change. The FE result—396.4 MPa at one location, most of the frame below 100 MPa—is the characteristic signature of a bending-dominated load path through a poorly placed geometric transition.

That extreme localisation is not an FE artefact. It is what happens when load transfer is forced through a bending-

dominated path at a geometrically constrained junction. The bracket junction concentrates both static yield and fatigue failure at the same location for the same reason; reorienting the load path addresses both.

4.1.2. Coupled Effect of Stress Concentration and Fatigue Nonlinearity

Stress concentration is where the geometry of the two designs diverges most at the local level. Design-1 has R/t = 1.25; Design-2 has R/t = 3.0. Using Peterson's charts for shoulder fillets under bending [35], those ratios correspond to $K_t \approx 2.8$ and $K_t \approx 1.9$ respectively—a 32% reduction. If Kt change were the only variable, the expected fatigue improvement under the IIW S–N slope of m = 3 would be $(2.8/1.9)^3 \approx 3.2$, or about a 69% damage reduction. The observed improvement is 99.9%—approximately 1,000×. That gap between 69% and 99.9% is not a modelling anomaly. It is the effect of the simultaneous reduction in mean stress and RMS amplitude, which compound with the Kt improvement because all three enter the same nonlinear S–N damage integral.

(1) Design-1: r/t = 5/4 = 1.25

(2) Design-2: r/t = 12/4 = 3.0

Based on Peterson's stress concentration charts for flat plates with shoulder fillets under bending [35], the corresponding theoretical stress concentration factors are approximately:

(1) Design-1: $K_t \approx 2.8$

(2) Design-2: $K_t \approx 1.9$

This represents a 32% reduction in Kt.

If this reduction were acting alone, the expected fatigue damage reduction under the IIW S–N slope (m = 3) [25] would be:

$$1 - (1.9/2.8)^3 \approx 69\% \quad (9)$$

However, the observed damage reduction exceeds 99%. This discrepancy reveals that the improvement mechanism is not merely geometric smoothing; rather, it arises from the combined effect between:

(1) Reduced stress concentration

(2) Lower dynamic stress amplitude

(3) Reduced mean stress level

(4) Improved load-path alignment

Kt correction alone accounts for a 69% damage reduction. The extra 30+ percentage points come from the lower mean stress and reduced RMS amplitude that the same geometric change also produces. These three effects are not separable in practice—they arise together from a single design decision—which is why evaluating them in isolation underestimates the total improvement.

4.1.3. Resonance Proximity and Dynamic Amplification

The first natural frequency of Design-1 (25 Hz) lies only 5 Hz above the dominant excitation band (5–20 Hz). Given typical 5–10% frequency scatter in welded steel assemblies [22], the effective separation margin may be further reduced in service.

Static compliance and fatigue safety are not equivalent—a point that Design-1 illustrates clearly. A structure can pass an ECE R110 yield check under quasi-static loading and still accumulate fatigue damage at a rate that would exhaust it long before a normal service life, if a natural frequency sits close to the dominant excitation band. Design-1 passes the lateral and vertical static checks with SF of 1.23 and 6.00 respectively. Adding the vibration fatigue calculation changes the picture considerably: D = 0.160 laterally and D = 4.424 longitudinally. A structure with those damage indices would not survive normal service, despite appearing mostly compliant under static analysis.

Modal position and fatigue outcome are closely linked in this structure. The 5 Hz separation between the first natural frequency and the upper edge of the high-energy excitation band contributes directly to the 106.6 MPa RMS stress, which in turn drives D = 4.424. Regulatory design practice focuses on quasi-static load cases; the present results suggest that modal positioning should be treated as an equally important parameter in preliminary design.

4.2. Mechanisms Underlying Reinforced Design Performance

4.2.1. Multi-Path Load Redistribution

Diagonal bracing aligned with the forward inertial vector converts a bending problem into an axial one. The plates still carry some load, but the diagonal members take the dominant share in direct tension—a far more efficient mechanism. The same geometry change also stiffens the frame, shifting natural frequencies away from the excitation band and reducing resonance amplification. So the 45.8% static improvement and the 39% RMS improvement are not separate achievements; they both come from the same structural change [36].

The 45.8% forward stress reduction and the 39% RMS improvement are not independent outcomes. Both follow from the same structural change—diagonal bracing converts the dominant load-transfer mechanism from bending to axial tension, simultaneously lowering peak static stress and reducing resonance amplification.

4.2.2. Integrated Reduction of Stress Amplitude and Mean Stress

The IIW FAT 90 S–N curve is derived at $R \approx 0.5$, so mean stress is already factored in. A Goodman-type overlay is not strictly required, but it helps visualise how far Design-2 has moved from the failure region.

Using $\Delta\sigma$ = RMS × $\sqrt{2}$ under Gaussian narrowband assumption:

Design-1 sits outside a simplified Goodman envelope; Design-2 sits comfortably inside it.

Design-2 shifts substantially closer to a moderate severity regime.

All three improvements follow from one geometric decision—the diagonal bracing and enlarged fillet:

(1) 39% reduction in RMS stress

(2) 46% reduction in static mean stress

(3) 32% reduction in Kt

Because damage $\propto \sigma^3$, those three reductions multiply. A factor of 0.61 in RMS, times a factor of 0.54 in mean stress, times a factor of $(1.9/2.8)^3$ in Kt—the product is less than 0.001. That explains the >99% damage reduction.

Each of the three stress-related quantities—mean, RMS amplitude, Kt—enters the damage sum as its own cubed contribution. Improving all three by the same factor compounds: three separate threefold improvements produce a 27-fold damage reduction, not a 3-fold one.

4.3. Design Implications for Hydrogen Cylinder Mounting Systems

The safety consequence of fatigue failure at the bracket–frame junction is worth stating explicitly. ECE R110 exists to ensure that hydrogen cylinders remain secured to the vehicle

under crash loading. A progressive fatigue crack at that junction—accumulated over months of normal road operation, long before any crash event—could compromise that assurance without triggering any inspection criterion. Design-1 passes two of the three ECE R110 static checks and would pass a visual inspection. What the static check cannot reveal is that the same design accumulates D = 4.424 longitudinally under the ISO 16750-3 road vibration spectrum. At the RMS stress levels driven by near-resonance amplification near 25 Hz, the structure exhausts its fatigue life in approximately 50 seconds of continuous PSD exposure. That is not a marginal compliance shortfall; it is a design that fails to achieve its primary safety function. Switching to Q460 steel raises the yield threshold but changes none of the three governing variables: Kt, load path orientation, or natural frequency. All three are determined by geometry.

4.4. Material Efficiency and Practical Implications

Q460 costs roughly twice Q345 in the Chinese structural steel market and requires more demanding preheat welding procedures. That cost premium might be acceptable if it resolved the problem. It does not. A Q460 frame with Design-1 geometry would still develop 396.4 MPa at the bracket junction—still above the Q460 yield stress of 460 MPa would not even apply, because the local stress is controlled by the geometry, not the material. The reinforced Q345 design achieves full compliance at lower procurement and fabrication cost by addressing the actual root cause rather than raising a threshold past it.

The practical implication is direct: when the root cause of failure is a stress concentration at a poorly oriented load path, upgrading the steel grade is the wrong intervention. Q345 at Q460 price does not buy what a bracket redesign at Q345 price does.

4.5. Transferable Design Guidelines for Hydrogen Cylinder Frames

The integrated results support the following design principles:

Guideline 1 — Prioritise axial load paths.

Primary members should align with dominant inertial vectors. Bending-dominated response under forward loading indicates inefficient structural topology.

Guideline 2 — Control geometric transitions.

Adopt fillet radii satisfying approximately R ≥ h/4 at major transitions and aim for fatigue notch factor K_f < 2.0 to avoid nonlinear fatigue amplification.

Guideline 3 — Limit static stress severity.

Maintain σ_{static} < 0.6σ_y to prevent excessive mean stress contribution to fatigue damage.

Guideline 4 — Manage modal separation.

Target first natural frequency >30 Hz to provide adequate separation from typical vehicle excitation peaks (5–20 Hz).

Guideline 5 — Avoid single-direction optimisation.

Ensure SF > 1.0 in all regulatory orientations; improvements in one axis must not introduce critical vulnerabilities in others.

The five guidelines above emerged from a specific 510 L dual-cylinder configuration, and some of the numerical thresholds—R ≥ h/4, σstatic < 0.6σy, first frequency above 30 Hz—are best treated as starting points for design rather than universal rules. The physical reasoning behind each guideline, however, is not specific to this system. It applies wherever inertial loads are large relative to the structural cross-section, where road vibration contributes meaningfully to fatigue, and where the bending stiffness of thin-walled members is a limiting factor—conditions that are common to many heavy-vehicle mounting applications.

4.6. Limitations and Future Research Directions

Six limitations should be acknowledged before extrapolating from these results.

First, the modal analysis presented here is complete only for Design-1. The fatigue calculation for Design-2 does incorporate its frequency response functions—so the dynamic response is accounted for in the damage results—but full natural frequency extraction and mode shape reporting for the reinforced configuration are absent. This is a genuine gap, not simply a presentation choice: knowing whether the first natural frequency of Design-2 has actually shifted above 30 Hz would strengthen the argument about resonance margin considerably.

Second, the lateral safety factor of Design-2 (SF = 1.03) satisfies the ECE R110 minimum, but only just. For a production implementation, that margin may prove insufficient once manufacturing tolerances and material property scatter are accounted for. The bracing geometry was optimised for the dominant forward direction; a second design iteration targeting lateral load redistribution would likely recover meaningful margin here.

Third, inertial load cases were analysed independently per ECE R110; combined multi-axial loading could introduce interaction effects not captured here.

Fourth, the FE models assume idealised geometry and homogeneous material properties throughout. Welding introduces residual stresses that can approach yield in the vicinity of the weld toe; heat-affected zone softening may reduce effective yield strength locally; dimensional variability will shift both static and dynamic responses from the nominal values. These effects were not explicitly modelled. For a comparative study where both configurations share the same material system and fabrication assumptions, this may be defensible—but the absolute fatigue life predictions should be treated with corresponding caution.

Fifth, the PSD fatigue calculation assumes stationary Gaussian random vibration. Non-stationary events—road bumps, speed humps, emergency braking—generate transient stress histories that Dirlik's method cannot capture. These are likely to be more damaging per cycle than the steady-state PSD would suggest.

Sixth, linear elastic assumptions were adopted. Plastic deformation in Design-1 was not modelled explicitly, which may influence absolute fatigue life predictions.

Future work should include:

(1) Experimental static validation testing
(2) Full modal characterisation of both configurations
(3) Accelerated vibration fatigue testing
(4) Nonlinear material modelling
(5) Multi-axial loading scenarios
(6) Topology optimisation studies
(7) Field-measured PSD spectrum incorporation

Experimental validation against the computational predictions is the most direct path to strengthening confidence in the framework. Accelerated fatigue testing under measured road PSD inputs would be particularly informative, given the nonlinear damage sensitivity identified here. Even a modest

strain-gauged test of the critical bracket junction under a realistic PSD excitation would provide meaningful validation of the FRF-based damage prediction approach.

4.7. Robustness of the Reinforced Configuration Under Parametric Variability

With D = 0.004 and SF = 1.61 as baselines, there is sufficient margin to ask whether the reinforced design would remain compliant under the kind of parameter variation that production manufacturing introduces. Three sources were examined: structural damping, plate thickness tolerance, and natural frequency scatter.

Structural damping variation within the typical range for bolted welded steel assemblies (ζ = 2–3% [22]) would modify resonance amplification factors but is unlikely to alter compliance status. With a fatigue damage index of D = 0.004 — 250 times below the failure threshold — even significant damping reduction would not approach the critical limit.

Manufacturing geometric variability at typical tolerance levels (±5% plate thickness) would proportionally affect local section modulus and stress magnitude. Given the cubic sensitivity of fatigue damage to stress amplitude under the IIW S–N slope (m = 3), a 5% stress increase would produce approximately 15.8% additional damage. Applied to D = 0.004, this yields D ≈ 0.005, remaining far below the D = 1.0 criterion.

Natural frequency scatter of 5–10% associated with manufacturing variability in welded assemblies [22] is expected to produce frequency shifts of the order of 1–3 Hz relative to the nominal design value. Given the upward frequency shift attributable to structural reinforcement (Section 3.5), such scatter is unlikely to position the first natural frequency within the dominant excitation band (5–20 Hz).

Across all three variability scenarios, Design-2 remains well within compliance. The D = 0.004 baseline provides a margin that appears sufficient to absorb realistic manufacturing scatter without approaching the failure threshold. Whether that conclusion holds under more severe parameter combinations, or under combined variability across all three sources simultaneously, would require a more formal sensitivity analysis—a natural extension of this work.

5. Conclusions

This study addressed a question with direct practical implications: can bracket geometry revision alone—with Q345 steel retained throughout—bring a structurally non-compliant hydrogen cylinder mounting frame into full regulatory and fatigue compliance? The short answer is yes. The longer answer is that the mechanism involves a nonlinear interaction between stress concentration, mean stress, and dynamic amplitude that makes geometry correction considerably more effective than material substitution for this class of failure.

5.1. Principal Technical Findings

5.1.1. Minimalist configuration limitations

The conventional Q345 tubular frame did not pass:

Maximum forward von Mises stress reached 396.4 MPa, exceeding Q345 yield strength (SF = 0.87).

The longitudinal vibration fatigue damage index (D = 4.424) exceeded the acceptance threshold.

The first natural frequency (25 Hz) provided limited separation from the dominant vibration energy band (5–20 Hz), enabling dynamic amplification.

Both failures trace to the same root cause: flat vertical plates in bending at a high-Kt junction, with the first natural frequency sitting 5 Hz above the dominant road excitation band. Correcting the load path geometry resolved both failures at once.

5.1.2. Reinforced configuration performance improvement

The reinforced frame passed all checks:

Maximum forward stress reduced to 214.8 MPa (45.8% reduction; SF = 1.61).

Fatigue damage index decreased to 0.004 (>99% reduction), providing approximately 250× margin relative to the failure threshold.

The improvement was achieved without material upgrading, using standard Q345 structural steel.

5.1.3. Nonlinear fatigue sensitivity

The scale of the fatigue improvement—three orders of magnitude—is explained by the m = 3 damage exponent of the FAT 90 weld class. When RMS stress, mean stress, and Kt all decrease together, the damage reductions multiply rather than add.

5.2. Methodological Contribution

Running modal extraction, static strength verification, and PSD fatigue assessment on a single consistent FE model is what makes the causal chain between resonance proximity and fatigue damage visible. Isolated analyses cannot provide this. The modal result in Section 3.1 explains the dynamic amplification in Section 3.3; the static result explains why mean stress enters the fatigue integral at an unfavourable level. These connections are only apparent when all three analyses share the same mesh, boundary conditions, and material definitions.

(1) Modal positioning analysis

(2) Regulatory static load verification

(3) Frequency-domain random vibration fatigue assessment

Static analysis alone shows Design-1 passing two of three load cases. Adding the fatigue calculation reveals D = 4.424 longitudinally and D = 0.160 laterally—a structure that would not survive normal service despite appearing mostly compliant under static checks.

5.3. Engineering Implications

Bracket geometry, not steel grade, determined the outcome. Three implications follow for engineers working on similar structures:

First, static compliance and fatigue safety are not equivalent

(1) Efficient axial load transmission reduces bending-dominated stress concentration.

(2) Minimisation of RMS stress under random vibration loading is critical due to cubic S–N sensitivity.

(3) Modal frequency separation from dominant excitation bands should be treated as a primary design parameter.

These three points are not specific to the 510 L dual-cylinder system examined here. They apply to any mounting structure where inertial mass is large, regulatory crash-loading governs the structural layout, and road vibration accumulates fatigue over years of service—conditions that describe a significant portion of heavy vehicle structural

design.

With $D = 0.004$ and $SF = 1.61$, the reinforced design has enough margin to tolerate normal manufacturing variation in plate thickness, damping, and natural frequency without losing compliance.

5.4. Final Statement

The central result is this: $D = 4.424$ was reduced to $D = 0.004$, and SF improved from 0.87 to 1.61, by adding diagonal bracing, widening fillets from $R = 5$ mm to $R = 12$ mm, and realigning the bracket—with Q345 steel retained throughout. Whether that result generalises beyond this specific configuration, and whether it holds under the non-stationary loading and weld quality variation that field conditions introduce, are questions experimental validation should address. For engineers working on similar systems: run the modal and fatigue analysis before the bracket geometry is fixed. The static check alone will not reveal the fatigue problem, and the geometry you specify will determine durability far more than the steel grade.

The analytical sequence—FE modal extraction, ECE R110 static verification, ISO 16750-3 PSD fatigue—is executable at the preliminary design stage, requiring only cylinder mass and chassis attachment geometry as inputs. No physical prototype is needed. It can therefore inform geometric decisions before tooling is committed, which is precisely when the bracket load path is easiest and cheapest to change.

Acknowledgement

This work was supported by the National Natural Science Foundation of China (Grant No. 52575058).

References

[1] Bethoux O. Hydrogen fuel cell road vehicles: State of the art and perspectives. Energies. 2020;13(21):5843.

[2] Ajanovic A, Haas R. Prospects and impediments for hydrogen fuel cell buses. Energy. 2021; 235:121340.

[3] Nguyen HQ, Shabani B. Review of carbon-based and carbon-free energy technologies for sustainable transportation. Renewable and Sustainable Energy Reviews. 2024; 173:113084.

[4] Zheng J, Liu X, Xu P, et al. Development of high pressure gaseous hydrogen storage technologies. International Journal of Hydrogen Energy. 2012; 37(1):1048–1057.

[5] Barthelemy H, Weber M, Barbier F. Hydrogen storage: Recent improvements and industrial perspectives. International Journal of Hydrogen Energy. 2017; 42(11):7254–7262.

[6] ECE R110. Uniform Provisions Concerning the Approval of Specific Components of Motor Vehicles Using Compressed Natural Gas (CNG) in their Propulsion System. United Nations Economic Commission for Europe; 2015.

[7] Farhangdoost K, Zamani M. Fatigue life assessment of automotive components under random loads. Journal of the Brazilian Society of Mechanical Sciences and Engineering. 2016; 38:295–304.

[8] Liu Y, Wang X, Du W. Cost analysis of high-strength steel application in automotive structural components. Materials & Design. 2019; 165:107583.

[9] Züttel A, Borgschulte A, Schlapbach L, eds. Hydrogen as a Future Energy Carrier. John Wiley & Sons; 2011.

[10] Elberry AM, Thakur J, Santasalo-Aarnio A, Larmi M. Large-scale compressed hydrogen storage as part of renewable electricity storage systems. International Journal of Hydrogen Energy. 2021; 46(29):15671–15690.

[11] Rivard E, Trudeau M, Zaghib K. Hydrogen storage for mobility: A review. Materials. 2019; 12(12):1973.

[12] Zohuri B. Hydrogen Energy: Challenges and Solutions for a Cleaner Future. Springer; 2019.

[13] Zheng J, Xu P, Liu P, et al. Optimization design of Type III hydrogen pressure vessel for fuel cell vehicle. Journal of Zhejiang University-SCIENCE A. 2012; 13(5):323–334.

[14] Barthelemy H. Hydrogen storage — industrial prospectives. International Journal of Hydrogen Energy. 2012; 37(22):17364–17372.

[15] Kim SC, Lee JH, Moon YH, et al. Finite element analysis of Al/CFRP composites for type III hydrogen pressure vessels. Composite Structures. 2010; 92(11):2708–2715.

[16] Rafiee R, Torabi MA. Stochastic prediction of burst pressure in composite pressure vessels. Composite Structures. 2018; 185:573–583.

[17] Li Y, Zhu Y, Lu Z, Guo J. Frequency domain methods for fatigue damage assessment under stationary Gaussian random loading. Fatigue & Fracture of Engineering Materials & Structures. 2022; 45(7):1885–1900.

[18] Benasciutti D, Tovo R. Spectral methods for lifetime prediction under wide-band stationary random processes. International Journal of Fatigue. 2005; 27(8):867–877.

[19] Bishop NW, Sherratt F. Finite Element Based Fatigue Calculations. NAFEMS Ltd; 2000.

[20] Wang L, Liang C, Zhang D, Chen J. Structural design and analysis of composite hydrogen storage cylinders for fuel cell vehicles. International Journal of Hydrogen Energy. 2018; 43(44):20336–20346.

[21] Kim JH, Lee JM, Kim J. Optimization of composite cylinder subjected to internal pressure and axial load. Journal of Composite Materials. 2018; 52(17):2355–2366.

[22] Lalanne C. Mechanical Vibration and Shock Analysis, Random Vibration (Vol.3). John Wiley & Sons; 2014.

[23] Lalanne C. Mechanical Vibration and Shock Analysis, Fatigue Damage (Vol.4). John Wiley & Sons; 2014.

[24] Tovo R. Cycle distribution and fatigue damage under broad-band random loading. International Journal of Fatigue. 2002; 24(11):1137–1147.

[25] Hobbacher AF. Recommendations for Fatigue Design of Welded Joints and Components (2nd ed.). Springer; 2016. (IIW document IIW-2259-15)

[26] Budynas RG, Nisbett JK. Shigley's Mechanical Engineering Design (10th ed.). McGraw-Hill Education; 2015.

[27] Bathe KJ. Finite Element Procedures. Prentice Hall; 2006.

[28] Bendat JS, Piersol AG. Random Data: Analysis and Measurement Procedures (4th ed.). John Wiley & Sons; 2011.

[29] Newland DE. An Introduction to Random Vibrations, Spectral & Wavelet Analysis (3rd ed.). Dover Publications; 2012.

[30] ISO 16750-3. Road vehicles — Environmental conditions and testing for electrical and electronic equipment — Part 3: Mechanical loads. ISO; 2012.

[31] Dirlik T. Application of Computers in Fatigue Analysis. PhD Thesis, University of Warwick; 1985.

[32] Miner MA. Cumulative damage in fatigue. Journal of Applied Mechanics. 1945; 12(3): A159–A164.

[33] HBM nCode. DesignLife User Manual. 2022.

[34] Bendsøe MP, Sigmund O. Topology Optimization: Theory, Methods, and Applications. Springer; 2003.

[35] Pilkey WD, Pilkey DF. Peterson's Stress Concentration Factors (3rd ed.). John Wiley & Sons; 2008.

[36] Michell AGM. The limits of economy of material in frame-structures. Philosophical Magazine. 1904; 8(47):589–597.

[37] GB/T 1591-2018. High strength low alloy structural steels. Standardization Administration of China; 2018.

[38] GB/T 700-2006. Carbon structural steels. Standardization Administration of China; 2006.

[39] Altair Engineering. HyperWorks Suite Documentation. Troy, MI; 2023.